Highly asymmetric magnetic domain wall propagation due to coupling to a periodic pinning potential

Journal:	*Journal of Physics D: Applied Physics*
Manuscript ID:	JPhysD-104368
Manuscript Type:	Paper
Date Submitted by the Author:	15-Dec-2014
Complete List of Authors:	Novak, Rafael; Universidade Federal de Santa Catarina, Campus Blumenau; Universite de Paris-Sud, Laboratoire de Physique des Solides Metaxas, Peter; The University of Western Australia, School of Physics Jamet, Jean-Pierre; Universite de Paris-Sud, Laboratoire de Physique des Solides Weil, Raphael; Universite de Paris-Sud, Laboratoire de Physique des Solides Ferre, Jacques; Universite de Paris-Sud, Laboratoire de Physique des Solides Mougin, Alexandra; Universite de Paris-Sud, Laboratoire de Physique des Solides Rohart, Stanislas; Universite de Paris-Sud, Laboratoire de Physique des Solides Stamps, Robert; University of Glasgow, School of Physics and Astronomy Zermatten, Pierre-Jean; CEA Grenoble, SPINTEC Gaudin, Gilles; CEA Grenoble, SPINTEC Baltz, Vincent; SPINTEC, Univ. Grenoble Alpes / CNRS / CEA Rodmacq, Bernard; CEA/DRFMC/SPSMS/MRS; SPINTEC, Univ. Grenoble Alpes / CNRS / CEA
Article Keywords:	Domain wall, Magnetization reversal, Magnetic multilayers, Domain structure, Domain wall pinning, Magneto-optical microscopy
Abstract:	Magneto-optical microscopy and magnetometry have been used to study magnetization reversal in an ultrathin magnetically soft $[Pt/Co]_2$ ferromagnetic film coupled to an array of magnetically harder $[Co/Pt]_4$ nanodots via a predominantly dipolar interaction across a 3 nm Pt spacer. This interaction generates a spatially periodic pinning potential for domain walls propagating through the continuous magnetic film. When reversing the applied field with respect to the static nanodot array magnetization orientation, strong asymmetries in the wall velocity and switching fields are observed. Asymmetric switching fields mean that the hysteresis of the film is characterized by a large bias field of dipolar origin which is linked to the wall velocity asymmetry. This latter asymmetry, though large at low fields, vanishes at high fields where the domains become round and compact. A field-polarity-controlled transition from dendritic to compact faceted domain structures is also seen at low field and a model is proposed to interpret the transition.

1
2
3
4
5
6
7
8
9
10
11
12
13
14
15
16
17
18
19
20
21
22
23
24
25
26
27
28
29
30
31
32
33
34
35
36
37
38
39
40
41
42
43
44
45
46
47
48
49
50
51
52
53
54
55
56
57
58
59
60

SCHOLARONE™
Manuscripts

Highly asymmetric magnetic domain wall propagation due to coupling to a periodic pinning potential

R L Novak[1]‡, P J Metaxas[2,3], J -P Jamet[1], R Weil[1], J Ferré[1], A Mougin[1], S Rohart[1], R L Stamps[2,4], P -J Zermatten[5], G Gaudin[5], V Baltz[5] and B Rodmacq[5]

[1] Laboratoire de Physique des Solides, Université Paris-Sud 11, CNRS, UMR 8502, F-91405 Orsay Cedex, France

[2] School of Physics, M013, University of Western Australia, 35 Stirling Highway, Crawley WA 6009, Australia

[3] Unité Mixte de Physique CNRS/Thales, 1 Avenue A. Fresnel, 91767 Palaiseau and Université Paris-Sud 11, 91405, Orsay, France

[4] SUPA – School of Physics and Astronomy, University of Glasgow, G12 8QQ Glasgow, United Kingdom

[5] SPINTEC, UMR-8191, CEA-INAC/CNRS/Univ. Grenoble Alpes, 38000 Grenoble, France

E-mail: `rafael.novak@ufsc.br`

Abstract.   Magneto-optical microscopy and magnetometry have been used to study magnetization reversal in an ultrathin magnetically soft $[Pt/Co]_2$ ferromagnetic film coupled to an array of magnetically harder $[Co/Pt]_4$ nanodots via a predominantly dipolar interaction across a 3 nm Pt spacer. This interaction generates a spatially periodic pinning potential for domain walls propagating through the continuous magnetic film. When reversing the applied field with respect to the static nanodot array magnetization orientation, strong asymmetries in the wall velocity and switching fields are observed. Asymmetric switching fields mean that the hysteresis of the film is characterized by a large bias field of dipolar origin which is linked to the wall velocity asymmetry. This latter asymmetry, though large at low fields, vanishes at high fields where the domains become round and compact. A field-polarity-controlled transition from dendritic to compact faceted domain structures is also seen at low field and a model is proposed to interpret the transition.

PACS numbers: 75.60.-d, 75.60.Ch, 75.78.Fg

‡ Present address: Universidade Federal de Santa Catarina, Campus Blumenau, Rua Pomerode 710, 89065-300, Blumenau, SC, Brazil.

Asymmetric magnetic domain wall propagation   2

1. Introduction

The magnetic stray field generated by an array of magnetically hard ferromagnetic nanodots can be used to create a periodically varying dipolar field-induced pinning potential for magnetic domain walls (DWs) moving in an underlying, continuous Pt/Co-based film or multilayer [1, 2]. This enables the generation of co-existent [3], yet structurally independent, periodic and disordered [4, 5] pinning potentials. While the former is mediated by the nanodots' stray magnetic field, the latter arises from inherent weak disorder in the continuous film. As such, the introduction of the periodic pinning potential does not perturb the structure nor the disorder of the continuous film [6] as opposed to methods involving patterning of the layer itself. [7, 8].

DW pinning from localised magnetic fields[9, 10, 11] generated by overlying nanodots[1, 2, 12, 13] depends on the relative alignment of the applied field driving wall motion and the orientation of the magnetization at saturation, M_{array}, of the nanodots within the array [1, 2, 12]. This not only introduces a new degree of freedom to control the pinning of DWs but also generates switching phenomena that are analogous [2, 14] to those induced by the unidirectional anisotropy in magnetic exchange bias systems [15, 16, 17, 18]. Both of these effects rely on the pinning potential for a given M_{array} being asymmetric under a switch of the polarity of the applied field used to drive the wall in the continuous magnetic film (or, equivalently, under a switch of M_{array} for a constant field polarity).

Beyond providing an attractive system for studying biasing effects and the interplay between distinct pinning potentials, the asymmetric pinning generated by the nanodots provides a way to locally pin DWs in a controllable and potentially reprogrammable fashion, thereby allowing one to control the propagation of DWs through nanodevices such as those recently proposed for high density magnetic data storage [19, 20] and DW logic [21] systems. However, while the asymmetries induced by nanodot arrays in the systems studied until now have been clearly measurable [1, 2], their relative weakness has made them unsuitable for practical application.

In this contribution, we show that it is indeed possible to generate strongly asymmetric magnetic reversal in coupled nanodot-film systems. The film stack is chosen so that it exhibits small intrinsic pinning effects and a reduced coercivity [5]. When coupled to an array of nanodots we evidence the following strong effects on magnetic reversal within the continuous film stack: (a) highly asymmetric hysteresis with a nanodot-induced order of magnitude increase in the coercivity; (b) differences of up to three orders of magnitude in DW velocities upon switching the field polarity, and (c) field-polarity-controlled transitions between compact faceted and percolation-like dendritic DW propagation modes.
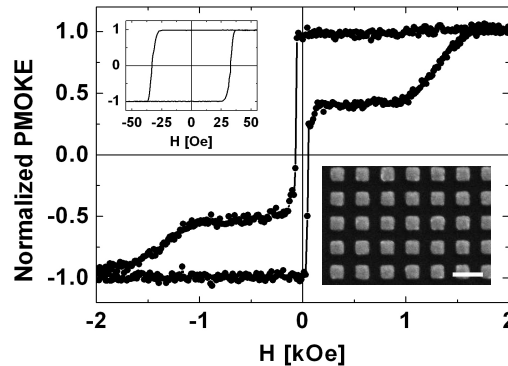
Asymmetric magnetic domain wall propagation   3

Figure 1. Room temperature normalized PMOKE hysteresis loop of the array and continuous film (field sweeping rate : 160 Oe/s). Upper inset: Conventional PMOKE hysteresis loop of the non-interacting part of the continuous film (40 Oe/s). Lower inset: Scanning electron microscopy (SEM) image of the nanodot array (the white scale bar is 500 nm long).

2. Sample structure and magnetic properties

Magnetically soft and hard Co/Pt-based multilayer stacks ($[Pt(2\ nm)/Co(0.45\ nm)]_2$ and $[Co(0.5\ nm)/Pt(2\ nm)]_4$ respectively) separated by a 3 nm thick Pt spacer layer were sputter deposited at room temperature onto a plasma-cleaned Si/SiO_2 substrate. The multilayer structure was designed to reduce the pinning and coercivity in both stacks. The thin 2 nm Pt layers separating the magnetic layers within each stack ensure that each stack behaves magnetically as a single ferromagnetic layer with different coercive fields. As intended, extraordinary Hall effect and polar magneto-optical Kerr effect (PMOKE) hysteresis loop measurements performed just after the film deposition show two well separated reversal jumps corresponding to the successive magnetization switching of the soft and hard stacks in the bilayer structure. The two multilayer stacks are relatively weakly coupled [22] across the Pt spacer, resulting in an effective ferromagnetic coupling field of 24 Oe acting on the magnetically soft stack. This field is one order of magnitude smaller than the dipolar fields acting on the layer after patterning the hard stack into an array of nanodots, and does not act along trenches formed between nanodots after patterning (see Sec. 3).

The upper, magnetically hard $[Co/Pt]_4$ stack was patterned via unfocussed Argon ion beam etching (IBE) through a hard Ti/Au mask fabricated using electron beam lithography and lift off. Etching was monitored via secondary ion mass spectrometry (SIMS) and halted upon reaching the Pt spacer layer so that 100 μm × 100 μm arrays of 0.2 μm wide ferromagnetic nanodots could be defined (figure 1, lower inset) while maintaining the structural integrity of the underlying magnetically soft $[Pt/Co]_2$ stack. A relatively large interdot separation of 0.2 μm ensures a negligible dipolar interaction between neighbouring nanodots. Both the continuous film stack and the nanodots retain their perpendicular magnetic anisotropy after patterning.

A conventional PMOKE hysteresis loop obtained with the field applied perpendicular to the film plane is shown in figure 1 wherein the sharp, low field switching of the soft continuous film and broad distribution of nanodot switching fields can both be identified. The top of the hysteresis loop is flat, indicating that the nanodots remain saturated upon removal of the magnetic field. The relatively high nanodot switching fields (between 1.0 and 1.5 kOe) ensure that the application of magnetic field pulses up to a few hundred Oe (used to switch the magnetization of the continuous film) does not affect the magnetic state of the nanodots. However, their switching fields are low enough to relatively easily reverse their magnetization, which is attractive for the creation of reprogrammable pinning sites.

3. Stray field pinning and bias generation

The out-of-plane magnetized nanodots radiate a strong perpendicular dipolar stray field component, H_{dip}^z, which acts on the underlying continuous film. Therefore, underneath the nanodot array, both the intrinsic weak disorder present in the continuous film and the nanodots' stray (or "fringing") field contribute to DW pinning. A 2D plot of H_{dip}^z at the centre of the continuous film is shown in figure 2(a) for down-magnetized nanodots ($M_{array} < 0$; the H_{dip}^z profile will be inverted for $M_{array} > 0$). Corresponding 1D plots are given (figure 2(b) and 2(c)) as calculated along a cross-section through the centres of two adjacent nanodots ($y = 100$ nm) and along a trench separating two nanodot rows ($y = 300$ nm). The applied field, H, used to drive DW motion can be either parallel (**P**) or antiparallel (**AP**) to M_{array}. The dipolar field component, H_{dip}^z, below nanodots has the same sign as M_{array}, while it exhibits the opposite sign beneath the trenches. It can thus be seen from figure 2 that, depending upon the lateral position of the DW within the continuous film and the sign of H, H_{dip}^z will either reinforce or compete with H. While the weak random disorder in the continuous film, which gives rise to DW creep at low fields [4], is insensitive to the field polarity, the nanodots stray field gives rise to a spatially periodic, field-polarity-dependent DW pinning potential. Furthermore, the abrupt polarity change in H_{dip}^z below the nanodot borders over a distance comparable to the DW width (~ 10 nm) can stabilize DWs at the nanodot edges which can make domain expansion beneath the trenches energetically favourable[1].

A consequence of this field-polarity-dependent pinning is dipolar biasing [2], wherein field-asymmetric DW pinning leads to different switching (or 'coercive') fields for positive and negative applied fields, for a given M_{array}. This can be seen in figure 3, where we show 'minor' PMOKE hysteresis loops which probe magnetic reversal only within the continuous film, in the cases where the nanodot array is saturated in (a) positive ($M_{array} > 0$) or (b) negative ($M_{array} < 0$) sense. During these measurements the applied field range has been limited to avoid switching of the nanodots. A large horizontal bias shift with the same sign as M_{array} is observed in the minor loops and is a consequence of the coercive field of the **P** configuration, H_C^P, being much higher than H_C^{AP}, the coercive field in the **AP** configuration. As will be shown in the following, the **P** configuration
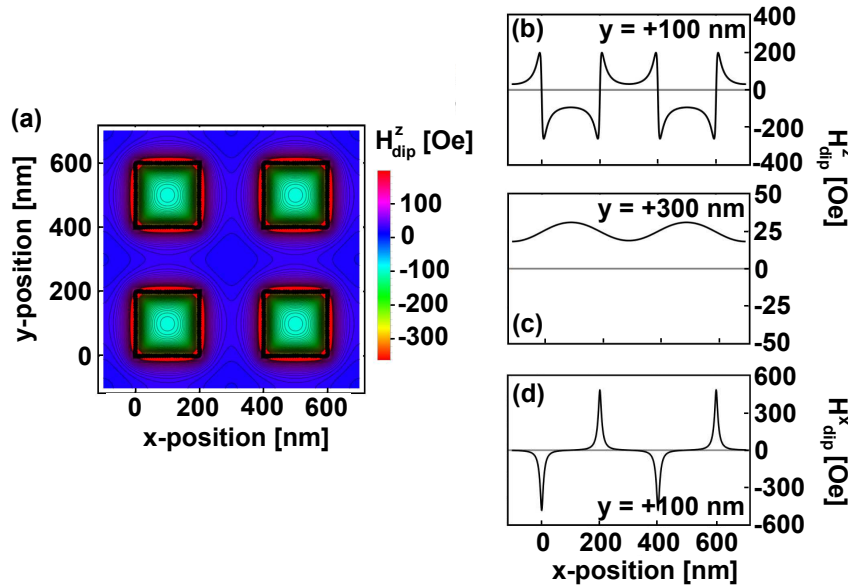
Asymmetric magnetic domain wall propagation

5

Figure 2. (a) 2D-plot of the perpendicular z-component of the stray field, H_{dip}^z, beneath four nanodots with width and separation of 200 nm, as calculated in the center of the continuous film. The nanodots are magnetized perpendicular to the film plane ($M_{array} < 0$). Each layer within the stack is assumed to be uniformly magnetized out of the film plane. The fields generated by the magnetic 'charges' on the upper and lower interfaces of the Co(0.5 nm) layers within the stack have been summed. The saturation magnetization of the Co layers was assumed to be 900 emu/cm³ [[5]]; (b) 1D plot of H_{dip}^z along a line ($y = 100$ nm) passing through the centres of adjacent nanodots; (c) 1D plot of H_{dip}^z along a line ($y = 300$ nm) passing through the central axis of the trench between nanodots; (d) 1D plot of the in-plane component of H_{dip} along a line ($y = 100$ nm) passing through the centres of adjacent nanodots. (Color online).

leads to a stronger DW pinning which hampers magnetic reversal in that branch of the loop, thus leading to an increased H_C^P. The magnetization reversal asymmetry, estimated from the ratio $H_B/H_C = 0.69$ of the bias field, $H_B = 29$ Oe ± 2 Oe, to the mean coercive field $H_C = (H_C^P + H_C^{AP})/2 = 42$ Oe ± 2 Oe, is much higher in the present case as compared to its value, 0.064, in arrays with the same size/separation ratio for nanodots studied in a previous work [2].

The remainder of the article will be mainly concerned with DW propagation underneath the arrays in the **P** and **AP** configurations. The phenomena described in the previous paragraphs (i.e. asymmetric DW pinning leading to bias and enhanced coercivity) are directly linked to the interactions between propagating DWs and the nanodot array [2]. For the **AP** configuration, H_{dip}^z assists field-driven DW motion below the trenches, while the opposite situation prevails for a **P** configuration. This picture of DW motion aided or hampered by H_{dip}^z depending on the lateral position of the DW within the continuous film and below the trenches will be developed in the following
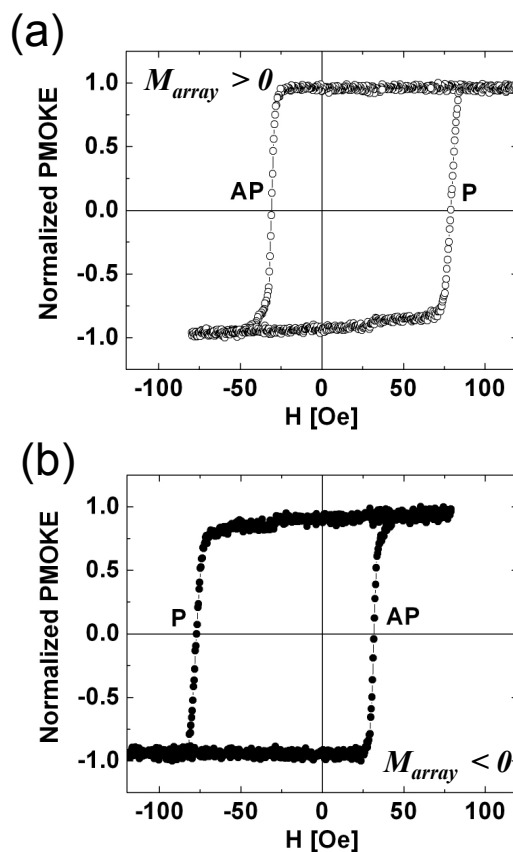
Figure 3. Horizontally shifted minor hysteresis loops of the continuous film beneath the array measured via conventional laser-based PMOKE magnetometry focused on the nanodot array through a 50 μm wide pinhole at a field sweep rate of 90 Oe/s for (a) $M_{array} > 0$; (b) $M_{array} < 0$.

sections in order to interpret the experimental observations.

4. Low field magnetic reversal mechanisms and domain structures

4.1. Remanent hysteresis loops obtained with PMOKE microscopy

Quasi-static PMOKE microscopy with high spatial resolution (~ 300 nm) was performed using a green LED ($\lambda = 505$ nm). This was used to follow the evolution of the remanent magnetic domain structure as a function of field, thereby obtaining remanent minor hysteresis loops which characterize switching in the continuous film both beneath and outside the arrays. The remanent loops were traced out by measuring a spatially averaged PMOKE signal from images recorded in zero field following consecutively applied field pulses with increasing/decreasing amplitude, H. As opposed to PMOKE magnetometry (figure 3), this microscopy-derived method enables a direct correlation between the magnetic state of the film and its domain structure.

The procedure is shown schematically in figure 4. Let us consider the field-induced
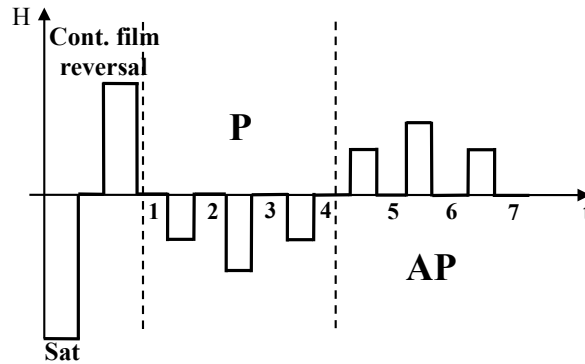
Figure 4. Experimental procedure used to determine the remanent hysteresis loops shown in Figure 5. Only a few field pulses are displayed in order to describe the protocol in a simple manner. The duration of each field pulse was 5 s, while the acquisition time of each image (at Positions 1 to 7) was 40 s. The detailed experimental procedure is reported in the text.

magnetic behaviour of the film located beneath the array. First, the sample is submitted to a large negative field (~ -2 kOe) in order to saturate the magnetization of both the nanodots ($M_{array} < 0$) and the continuous film, see $M(H)$ data in figure 1 (Sat state in figure 4). Following this saturation step, a $H = +200$ Oe field pulse with 5 s duration is applied to saturate the magnetization of the continuous film in the "up" orientation (Second step in figure 4).

$H < 0$ pulses with increasing amplitude are then successively applied, followed by the acquisition of PMOKE images of the frozen remanent state for increasing H (e.g. Positions 2 and 3 in figure 4). The negative field eventually leads to nucleation of reversed domains. This typically occurs outside the array resulting in a domain wall which propagates towards the array, eventually penetrating it. After reaching the saturation of the film under negative field ("down" orientation), the field is stepped back to zero and the process is repeated for pulses with $H > 0$. Referencing figure 4, remanent images captured in Positions 2 and 3 (5 and 6) refer to the **P** configuration (**AP** configuration).

By following the protocol outlined above, PMOKE images corresponding to intermediary remanent states during the magnetization reversal of the continuous film are obtained from the difference between images acquired immediately after applying a field pulse leading to domain wall propagation (e.g. position 2 in figure 4) and a reference image acquired at Position 1 before a domain wall has propagated into the microscope field of view. The images, shown in Figs. 5 and 6 cover a wide region of the sample including a corner of the array. Remanent hysteresis loops were constructed by spatially averaging the PMOKE signal over 12 μm x 6 μm regions located either outside or beneath the nanodot array[2] (figure 5).

Note that a square and symmetric remanent hysteresis loop with low coercivity, $H^0_{C,prop} = 8 \pm 2$ Oe is obtained outside the array where smooth domain walls propagate easily through the film up to the array edge (figure 5, dashed line). In contrast, the loop
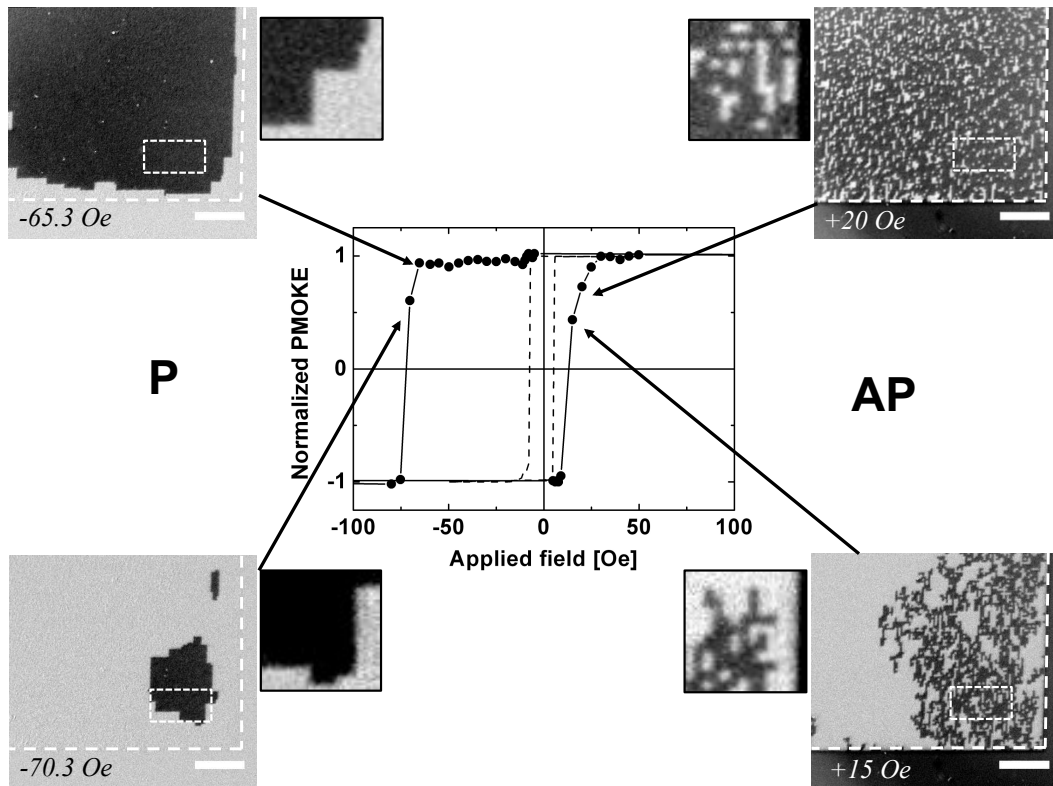
Figure 5. At the center: local PMOKE minor wall propagation-assisted hysteresis loop of the continuous film measured outside (dashed line) or underneath (continuous line and closed dots) the 200/200 nanodot array (magnetically saturated in the 'down' direction $M_{array} = -M_{sat}$). After each field pulse, applied during 5 s, the normalized remanent magnetization is deduced from the integrated PMOKE remanent signal over an area delimited by the small white dashed rectangle (see images). The array is delimited by heavy white dashed lines. The size of the scale bars is 10 μm. Detailed views of selected areas of the main snapshot images are shown in associated smaller images (size: 5.4 μm x 5.4 μm).

obtained beneath the array is highly asymmetric (figure 5, solid line), consistent with the data in figure 3(b). Reversal in each branch is mediated by vastly different modes of domain wall propagation as can be seen in the domain snapshots also shown in figure 5: dendritic domain expansion in the low-coercivity **AP** branch and compact square domains in the high coercivity **P** branch. The coercivities for **P** and **AP** configurations measured from this loop are: $H_{prop}^{P} = 69 \pm 6$ Oe, $H_{prop}^{AP} = 13 \pm 2$ Oe.

　　In the following, a complete description of the mechanisms governing the observed magnetization reversal process will be presented. This description is based on the subdivision of the continuous film in (200 nm x 200 nm) cells, as shown in figure 7. Four different kinds of cells are defined, according to their positions with respect to the nanodot array: cells lying immediately below nanodots (**Dot** cells) are represented in black, cells located below trenches separating nanodots along the array border are hatched and denoted by **B**, cells situated below trenches inside the array are called **S**
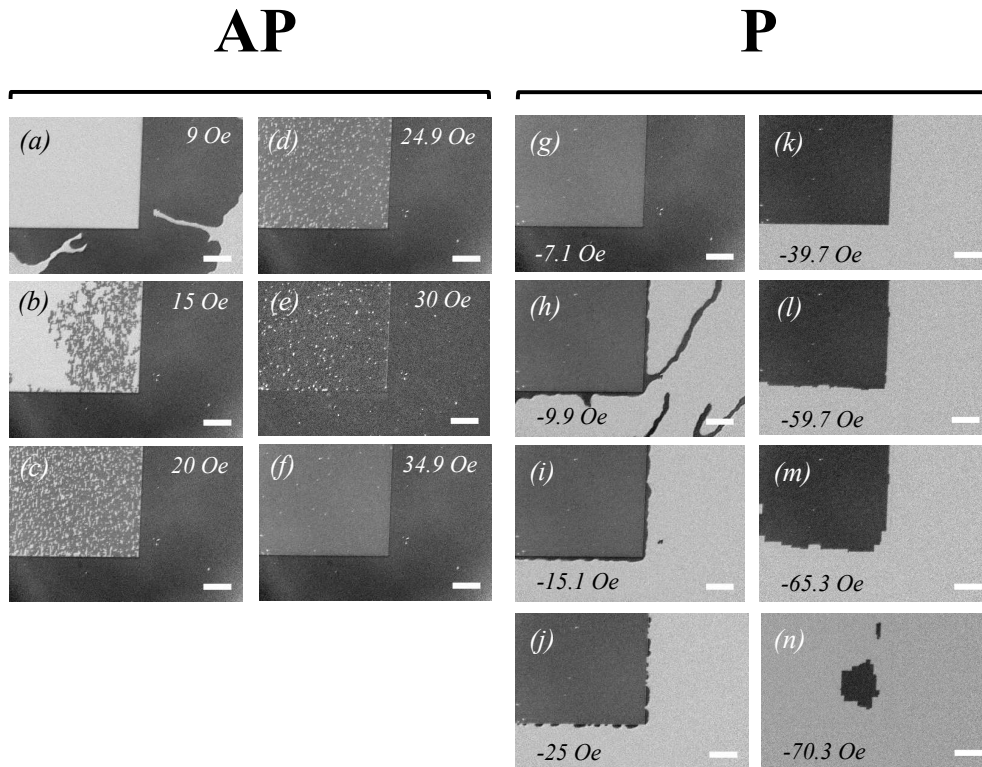
Asymmetric magnetic domain wall propagation   9

Figure 6. Remanent domain state of a part of the film located beneath (upper left side of the images) and outside (lower left and right side of the images) the array, obtained after applying a negative (**P** configuration) or positive (**AP** configuration) field with increasing absolute value, during 5 s. The **AP** configuration is shown in the left-hand panels ((a) – (f)) and the **P** configuration in the panels at the right-hand side ((g) – (n)). The size of the white scale bars is 10 μm).

(light gray), and cells located below the intersection area of two orthogonal trenches are denoted **I** cells and represented in dark gray. These cells will play different roles in the domain wall propagation process in **P** and **AP** configurations, which will be the subject of the next sections.

4.2. *AP configuration*

In the **AP** configuration, we start with both the nanodot array and the continuous film down-magnetized ($M_{array} < 0$, $M_{film} < 0$). Reversal occurs via expansion of a positively magnetised domain under a field $H > 0$. This propagating domain wall rapidly moves to the array boundary and penetrates it at a field of $\sim$ 12 Oe (first moving into **B** cells, figure 7). This is low compared to the penetration field of $\sim$ 65 Oe for the **P** configuration (see Sec. 4.3). Notice that the invasion of **B** cells does not occur simultaneously all around the array, but only in certain locations (figure 6(b)). We ascribe this to local disorder at the array periphery caused by the nanofabrication
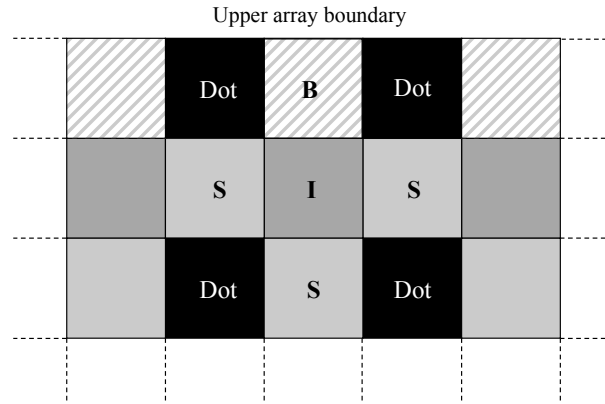
Figure 7. Diagram of a region of the sample divided in cells. The projection of the square dots on the continuous film is represented in black. The upper boundary of the array is located at the top of this figure. The film is divided in different types of square cells (cell side = 200 nm): **B**, at the array border (hatched), **I** located beneath the intersection of two trenches, and **S** located beneath trenches separating nanodots.

215 process. To understand this, we consider the stray field generated by the nanodots.
216 The stray field beneath the nanodots will repulse the expanding domain since there,
217 $H^z_{dip} < 0$. However, around the nanodots, H^z_{dip} is positive and aligned with the field
218 driving the domain wall propagation. This alignment means that the propagating wall
219 which marks the boundary of the expanding up-magnetised domain is attracted to the
220 border of each nanodot[2]. The stray field thus helps to drive (i) motion of the domain
221 wall up to the array border, as well as the subsequent (ii) penetration into the array
222 and (iii) propagation beneath the trenches which separate rows of antidots (in all these
223 positions H^z_{dip}, like H, is positive). We point out that isolated nucleation events within
224 the array (in **S** or **I** cells) were not observed before the penetration of domain walls
225 from the array borders (**B** cells). This means that it is harder to nucleate a single **S/I**
226 cell than to switch its magnetization through the propagation of a domain wall from an
227 adjacent cell. In order to nucleate a single reversed **S** cell, four new domain walls must
228 be created around the cell (along the nanodot periphery), costing more energy than the
229 two new domain wall segments added to the adjacent domain would cost.

230   We can thus consider motion in the **AP** configuration as a dendritic growth mode
231 through the connected, overlapping trenches lying between the nanodots (**S** and **I** cells,
232 figure 7). Notice that domains expanding from **I** cells may follow either a straight path or
233 turn 90° towards adjacent **S** cells. The images show a predominance of straight dendrites
234 in the **AP** configuration, which can be explained by magnetostatic considerations
235 within the film plane (90° branches have higher demagnetizing field). This process
236 leads to the formation of the observed dendrites (figure 6(b)). It is possible to find
237 positions in the array where there are closely spaced dendrites propagating in the same
238 direction (figure 8(a)). Measurements of the image intensity over the two dashed lines
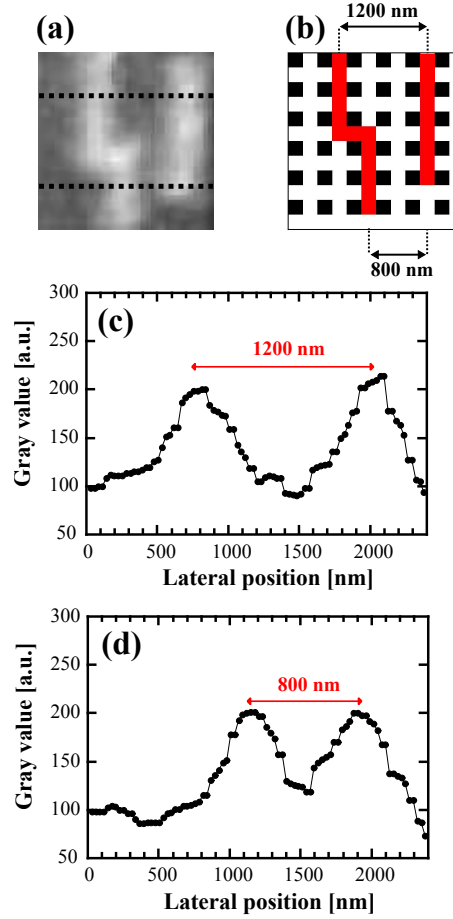
Asymmetric magnetic domain wall propagation   11

Figure 8. Domain propagation during dendritic growth in the **AP** configuration. (a) Detailed view (2.2 μm x 2.2 μm) of the domain structure in figure 5, right; (b) proposed dendrite structure as inferred from (a); (c) and (d) mean gray values measured along the two dashed lines in (a).

in figure 8(a) (see figure 8(b,c)) show that the dendrites are spaced by multiples of 400 nm (i.e. the period of the array). This is consistent with dendrite motion through the attractive trench regions, as shown in the schematic of figure 8(d).

We propose that this dendrite formation is followed by reversal underneath the nanodots. Indeed, neglecting disorder, the energy of an isolated down-magnetised domain stabilised beneath a nanodot by the local H_{dip}^z-induced Zeeman energy, E_Z ($E_{domain} = E_{DW} + E_Z(H_{dip}^z)$ with $E_Z(H_{dip}^z) < 0$), is about two times higher than the energy corresponding to a uniform magnetisation due to the high energy of the domain wall, E_{DW}, which borders the down-magnetised domain ($E_{uniform} = E_Z(H_{dip}^z)$ where $E_Z(H_{dip}^z) > 0$).

4.3. **P** configuration

In the initial state for the **P** configuration (Position 1, figure 4), all the nanodots are down-magnetized ($M_{array} < 0$) while the magnetization of the continuous film is up-

magnetized ($M_{film} > 0$). Under a weak negative field ($H < 0$), a down-magnetized domain nucleated far from the array propagates towards the array (figure 6(g)-(h)). In contrast to the **AP** case, the wall remains a considerable distance from the array boundary, even at $H \approx -15$ Oe, which is evidenced by the persistence of the up-magnetized decoration ring around the array (figure 6(i)). The ring is stabilized by the positive dipolar field H_{dip}^z present around the nanodots for $M_{array} < 0$ (figure 2), which in the **AP** case, led to an attraction of the domain wall to the nanodot edges.

For higher fields, this decoration ring shrinks to a series of bubbles that disappear for $H \approx -40$ Oe (figure 6(k)). However, it is not until we reach ~ -60 Oe that we have wide-scale penetration of domain walls into the array (figure 6(k)-(m)). This occurs via the expansion of straight edged domains, suggesting a row-by-row reversal within the array, in stark contrast to the dendritic reversal mode observed for the **AP** case. Intuitively however, one expects the reversal to be very different to the **AP** case: trenches which formed favourable paths for domain wall propagation in the **AP** case, now form a continuous repulsive region for domain growth in the **P** case. The repulsive H_{dip}^z beneath the trenches also forms a barrier to domain expansion underneath the nanodots where albeit, H_{dip}^z is aligned with the applied field making the nanodot-covered regions favourable for domain wall motion. Again, isolated nucleation events within the array were not observed before the penetration of domain walls from the array border.

The key point, however, is that domain walls must move below the trenches before reaching the regions beneath the nanodots. Once the trenches are switched however, reversal underneath the nanodots is, a priori, highly favourable due to the sign of H_{dip}^z in those regions. Despite the presence of an H_{dip}^z overshoot around the nanodot edges that can be higher than 200 Oe (figure 2(b)), we suggest that this happens spontaneously once the walls have propagated partly into the trench regions between the nanodots (**S** cell in figure 7), leading to avalanche-like row by row reversal. The effective energy barrier produced by this H_{dip}^z overshoot, whose calculated oscillation amplitude exceeds the driving field, might be notably reduced thanks to the in-plane dipolar field component present at the same location (Figure 2(d)), and because the oscillation expands over a distance of the order of the DW width. Thus, it is supposed that locally, around the nanodot edges, the effective H_{dip}^z value does not exceed 100 Oe, allowing the magnetization of the film to reverse quasi-instantaneously by DW motion beneath nanodots under the initial applied field of 200 Oe (figure 4).

4.4. Trench-mediated motion

Thus, in both configurations, we suggest that motion is dominated by domain wall propagation beneath the trenches. In the **AP** configuration, motion within the regions below continuous trenches is aided by H_{dip}^z leading to an easy dendritic reversal mode. The domain walls avoid the regions underneath the nanodots where H_{dip}^z is aligned against H which makes those regions repulsive to the expanding domain. In the

₂₉₂ **P** configuration, an expanding domain must pass below the repulsive trenches in order
₂₉₃ to reach the attractive regions beneath each nanodot. This occurs for fields around 60
₂₉₄ Oe, where wide scale penetration of domain walls into the array was observed (figure
₂₉₅ 6), so we take this value as the minimum field necessary to reverse a **Dot** cell.

₂₉₆   We thus argue that in both cases, a net forward movement of the domain wall
₂₉₇ front can occur only via domain expansion below the trenches. In a simple model, the
₂₉₈ magnitude of the field required for a domain wall to begin to move through the array
₂₉₉ can be written as:

$$H_{prop}^* = H_C^0 + H_{dendrite} \pm |H_{dip}^{Z,0}| \tag{1}$$

₃₀₁ where H_C^0 is the contribution from the intrinsic disorder (the coercivity outside the array
₃₀₂ which can be measured from figure 5), $H_{dendrite}$ is the field associated with the elastic
₃₀₃ energy increase due to a dendritic formation in an S cell and $H_{dip}^{Z,0}$ the local H_{dip}^z field
₃₀₄ within the trench. This latter term will be negative for the **AP** configuration where
₃₀₅ H_{dip}^z aids H and positive for the **P** configuration. Assuming $H_{dendrite}$ is the same for
₃₀₆ both configurations, we find that

$$H_{prop}^{P*} - H_{prop}^{AP*} = 2|H_{dip}^{Z,0}| \tag{2}$$

₃₀₈ Using the values obtained above for $H_{prop}^{P,AP}$, we have $H_{prop}^{P*} \approx 69$ Oe and $H_{prop}^{AP*} \approx 13$
₃₀₉ Oe, resulting in $|H_{dip}^{Z,0}| \approx 28 \pm 8$ Oe. This compares well to the field at the centre of
₃₁₀ the regions below trenches, providing some support for this simple, trench-mediated
₃₁₁ picture of domain wall motion. Note that there is some disorder in both growth modes,
₃₁₂ presumably due to intrinsic disorder within the continuous layer.

₃₁₃ *4.5. Comparison with other models*

₃₁₄ Lyberatos et al [23, 24] have compared a micromagnetic-cell based model with the
₃₁₅ microscopic random field Ising model (RFIM) and the random bond Ising model (RBIM)
₃₁₆ [25]. In both cases, the domain growth mode depends upon the ratio between either
₃₁₇ field or exchange fluctuations and the exchange integral, J. When disorder is rather
₃₁₈ large compared to J, a dendritic growth mode is observed, while as disorder decreases
₃₁₉ a transition to compact faceted growth is favoured. A qualitative analogy can be
₃₂₀ made to our system. The high disorder case corresponds to the **AP** configuration
₃₂₁ where the domain wall motion is determined by motion past isolated, disconnected
₃₂₂ repulsive positions (ie. high disorder). In contrast, in the **P** configuration, the domain
₃₂₃ wall motion is limited by its movement through connected repulsive regions (i.e. low
₃₂₄ disorder). Additionally, since the motion in the **AP** configuration can occur at lower
₃₂₅ fields, the motion is more susceptible to intrinsic disorder within the continuous film[5].

₃₂₆   In analogy to the RBIM, in the present case the exchange energy may be replaced
₃₂₇ by the coercivity that spatially fluctuates between **Dot** cells and trenches (**S** and
₃₂₈ **I** cells). Thus, the ratio between the fluctuation term and the propagation field
₃₂₉ along the trenches, given by the coercivity for each configuration, is certainly the

1
2
3
4
5
6
7
8
9
10
11
12
13
14
15
16
17
18
19
20
21
22
23
24
25
26
27
28
29
30
31
32
33
34
35
36
37
38
39
40
41
42
43
44
45
46
47
48
49
50
51
52
53
54
55
56
57
58
59
60

Asymmetric magnetic domain wall propagation   14

330 pertinent parameter that controls the wall propagation mode. In both configurations
331 the fluctuation term corresponds to the difference between the coercivity of a **Dot** cell
332 (estimated to be ~ 59 Oe) and of the coercivity in the trenches, about 68 Oe and 13
333 Oe in the **P** and **AP** configurations, respectively. This leads to ratios equal to 0.13 and
334 3.5, respectively, consistent with a transition from compact faceted to dendritic growth
335 modes in the framework of the RBIM, where such transition occurs for a ratio of 0.5[25].
336 A similar trend has been found in other works [23, 24, 26] in thin films with perpendicular
337 anisotropy, where the competition between DW and *intralayer* magnetostatic energies
338 were considered.

339 **5. Field-dependent domain morphology and short time dynamics**

340 In this section we examine the domain morphology and domain wall dynamics under
341 larger field magnitudes than in the previous section. To do this, nucleated domains were
342 expanded beneath the arrays using pulsed magnetic fields with duration t_{pulse}. When
343 increasing the field in the **AP** configuration , the low field percolating dendritic domain
344 structure ($H = 20$ Oe, $t_{pulse} = 5$ s, figure 9(a)) transforms under moderate field ($H = 52$
345 Oe, $t_{pulse} = 1$ ms, figure 9(b)) into a denser structure to give finally rise to nearly round
346 compact domains at much higher field ($H = 487$ Oe, $t_{pulse} = 1$ μs, figure 9(c)).
347   In the **P** configuration, the compact faceted domains observed in low field ($H = 73$
348 Oe, $t_{pulse} = 5$ s, figure 9(d)) transform first into domains with rougher DWs ($H = 112$
349 Oe, $t_{pulse} = 2$ ms, figure 9(e)). This indicates transition to a motion regime where
350 the intrinsic disorder within the film dominates the effect of the periodic H_{dip}^z. Finally,
351 nearly round shaped domains with smoother walls are observed at high fields ($H = 440$
352 Oe, $t_{pulse} = 200$ ns, figure 9(f)), similar to those seen in the **AP** configuration.
353   DW velocities can be deduced from the difference between remanent PMOKE
354 images captured over a small film area before and after the application of the magnetic
355 field pulse [5]. In the continuous film outside the array, a rather flat wall moves uniformly
356 and its velocity v is deduced from the ratio between the distance traveled by the DW and
357 the pulse duration [27]. The velocity can be determined in the same way for the dense
358 faceted structure observed in the **P** configuration. Conversely, in the **AP** configuration
359 the DW velocity due to dendritic domain growth is roughly estimated from the average
360 distance travelled by the front of the percolating magnetic pattern. Thus, the latter
361 gives a measurement of an upper bound for the velocity in the **AP** configuration.
362   In the continuous film outside the array, the field dependence of the DW velocity
363 exhibits good consistency with a creep law [4]:

$$v = v_0 exp\left[- \left(\frac{T_{dep}}{T}\right)\left(\frac{H_{dep}}{H}\right)^{1/4}\right]. \tag{3}$$

365 This is confirmed from a $\ln v$ versus $H^{-1/4}$ plot (figure 10(a)). Below the array, the
366 velocity is reduced by the dipolar coupling to the nanodots leading to a deviation from
367 Eq. (3). This nanodot-induced retardation is observed for both configurations with
368 the velocity reduction being significantly higher in the **P** configuration, consistent with
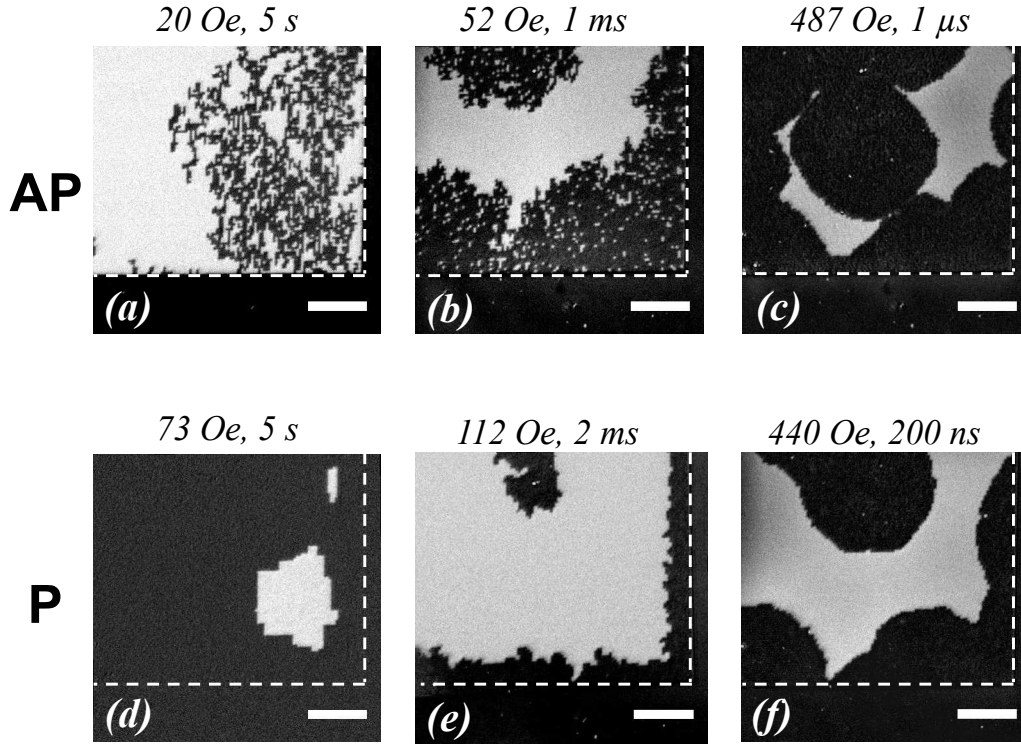
Figure 9. Evolution of reversed magnetic domains (in black) appearing underneath the nanodot array when increasing the applied field (and decreasing pulse duration) indicated above image snapshots for **AP** and **P** configurations. The size of the scale bars is 10 μm.

higher coercivity observed in Figs. 3 and 5. The ratio of the DW velocities measured for the **P** and **AP** configurations is shown in figure 10(b). At low field, wall motion is about three orders of magnitude slower in the **P** configuration.

Despite the crudeness of the DW velocity measurements for these domain structures, the DW retardation can be understood in terms of a configuration dependent, macroscopic retarding field, $H_{ret} > 0$, which acts uniformly against DW propagation [1, 2]. In the inset of figure 10(a) we show the $\ln v$ data plotted against $(H - H_{ret}^{P,AP})$ where $H_{ret}^{P} = 87$ Oe and $H_{ret}^{AP} = 24$ Oe. The plots indicate that there is a good overlap of the velocity data obtained inside and outside the array.

As mentioned in Section 3, a consequence of the asymmetric DW propagation modes in **P** and **AP** configurations is the occurrence of a large dipolar bias field, $H_B = 28 \pm 2$ Oe, arising from configuration dependent propagation fields ($H_{prop}^{P} = 69 \pm 6$ Oe, $H_{prop}^{AP} = 13 \pm 2$ Oe), both higher than that of the soft non-interacting continuous film ($H_{C,prop}^{0} = 8 \pm 2$ Oe) (figure 5). Contrary to previous results [2], the H_{prop}^{P} and H_{prop}^{AP} values are very different from each other and now closer to the retarding fields $H_{ret}^{P} = 87$ Oe and $H_{ret}^{AP} = 24$ Oe deduced from wall velocity measurements.

This result supports the relation $2H_B = (H_{prop}^{P} - H_{prop}^{AP}) = (H_{ret}^{P} - H_{ret}^{AP}) \approx 60 \pm 4$ Oe demonstrated and discussed in Appendix A. This large bias field, $H_{prop}^{B} = 28$
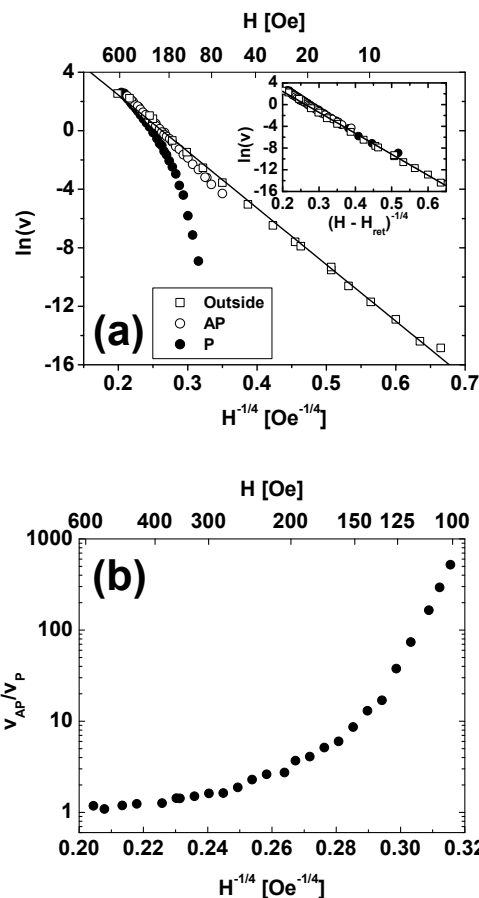
Figure 10. (a) Natural logarithm of the DW velocity v plotted against $H^{-1/4}$ in the continuous film outside (squares) and beneath the nanodot array for the **P** (full circles) and **AP** (open circles) configurations. Inset: $v(H - H_{ret})^{-1/4}$ plots for the **P** ($H_{ret}^P = 87$ Oe) and **AP** ($H_{ret}^{AP} = 24$ Oe) configurations can be superimposed on the creep plot of the continuous film ($H_{ret}^0 = 0$). The line in (a) corresponds to a linear fit to the continuous film data points. (b) Field dependent asymmetry in DW velocity for the **AP** and **P** configurations.

Oe ± 2 Oe, compared with the mean coercivity measured below the array, $H_{prop} = (H_{prop}^P + H_{prop}^{AP})/2 = 41 \pm 4$ Oe, is a consequence of the large asymmetry in DW propagation modes in **P** and **AP** configurations. $H_{prop}^{(P,AP)}$ are also much higher than $H_{C,prop}^0 = 8$ Oe (figure 5) for the non-interacting continuous film. Finally, as previously evidenced [2], no bias was found for a randomly demagnetized nanodot array, while the coercivity still remained larger than the coercivity of the continuous non-interacting film.

6. Conclusion

A soft ferromagnetic film submitted to a non-homogeneous dipolar stray field generated by an array of magnetized nanodots was investigated by PMOKE microscopy. We demonstrate asymmetries in the coercivity and low field-driven DW velocity when

Asymmetric magnetic domain wall propagation   17

reversing the applied field with respect to the fixed magnetization of an array of nanodots (**P** or **AP** configurations). These asymmetries are significantly higher than those seen previously in similar systems[2, 5]. At low field, the domain growth mechanism differs markedly for the **P** and **AP** configurations, with a sharp contrast between faceted domains on the **P** branch of the hysteresis loop and dendritic domains on the **AP** branch. A simple model of motion along the trenches between nanodots has been suggested which gives a reasonable match with our results. An analogy is also drawn with the case of the random field Ising model (RFIM), where a transition from faceted to dendritic domains is attributed to the increase of the ratio between randomness and coercivity, the former in our case attributed to the non-uniformity of the domain wall energy along different cells within the sample.

These results further demonstrate that nano-patterning can be used to design phenomenologically rich magnetic nanostructures and to switch rapidly the unidirectional anisotropy in a soft magnetic film without thermal treatment, as required in exchange biased systems. In judicious cases, the resulting bias could be exploited to easily drive DWs along trenches. Having the opportunity to initialize individually the magnetization state of each nanodot in a magnetic device with a field pulse, DWs could be driven by a fixed magnetic field through defined paths in the soft layer to finally reach addressed terminals.

Acknowledgments

Appendix A. Connection between creep and hysteresis loops

Our experimental results highlight direct links between creep and the quasi-static hysteresis loops. Starting from the expression (3) for the wall velocity in the creep regime for the non-interacting continuous film, we assume that the propagation coercivity, $H_{C,prop}^0$, corresponds to a field that drives the wall at a given velocity, v_d, so that half of the small probed film area is reversed after a single field pulse with duration equal to t_{pulse}. The expression for the wall-mediated coercive field for this portion of continuous film located outside the array can be written as :

$$H_{C,prop}^0 = (T_{dep}/T)^4 H_{dep}/[ln(v_d/v_0)]^4 \tag{A.1}$$

where $ln(v_d/v_0) < 0$. To determine $H_{C,prop}^0$, we prepare a wall at the border of the image and then step the field from $H = 0$ ($t_{pulse} = 5$ s) while measuring a local remanent

Asymmetric magnetic domain wall propagation   18

PMOKE loop over a small area located outside the array. The resultant remanent loop includes no contributions from nucleation and is shown in figure 5 as a dashed line. The finite wall propagation-assisted coercive field of $H^0_{C,prop} = 8$ Oe ± 2 Oe is due to pinning by intrinsic structural inhomogeneities in the continuous film.

A similar expression can be derived below the nanodot array:

$$H^{P(AP)}_{prop} = H^{P(AP)}_{ret} - (T_{dep}/T)^4 H_{dep}/[ln(v_d/v_0)]^4 \tag{A.2}$$

This expression shows that the coercive fields for **P** or **AP** configurations depend both on the intrinsic and periodic pinning potentials. Next, for measurements performed at the same field sweeping rate (or t_{pulse} value), we can derive the following two simple relations :

$$H^0_{C,prop} = H^P_{prop} - H^P_{ret} = H^{AP}_{prop} - H^{AP}_{ret} \tag{A.3}$$

$$2H^B_{prop} = (H^P_{prop} - H^{AP}_{prop}) = (H^P_{ret} - H^{AP}_{ret}) \tag{A.4}$$

Note that it is straightforward to check the relation (A.4) since remanent hysteresis loops in **P** and **AP** configurations are both performed at the same field sweeping rate (or t_{pulse} value) and dynamic data are extracted for the same wall velocity. However, since the pulse duration for dynamic measurements is not simply related to the field sweeping rate for hysteresis loops, it is more difficult to verify the expression (A.3). As a consequence, we have not checked this relation.

References

[1] P. J. Metaxas, P.-J. Zermatten, J.-P. Jamet, J. Ferré, G. Gaudin, B. Rodmacq, A. Schuhl, and R. L. Stamps. Periodic magnetic domain wall pinning in an ultrathin film with perpendicular anisotropy generated by the stray magnetic field of a ferromagnetic nanodot array. *Appl. Phys. Lett.*, 94(13):132504, 2009.

[2] P. J. Metaxas, P.-J. Zermatten, R. L. Novak, S. Rohart, J.-P. Jamet, R. Weil, J. Ferré, A. Mougin, R. L. Stamps, G. Gaudin, V. Baltz, and B. Rodmacq. Spatially periodic domain wall pinning potentials: Asymmetric pinning and dipolar biasing. *J. Appl. Phys.*, 113(7):073906, 2013.

[3] A. M. Ettouhami and L Radzihovsky. Velocity-force characteristics of an interface driven through a periodic potential. *Phys. Rev. B*, 67:115412, Mar 2003.

[4] S. Lemerle, J. Ferré, C. Chappert, V. Mathet, T. Giamarchi, and P. Le Doussal. Domain Wall Creep in an Ising Ultrathin Magnetic Film. *Phys. Rev. Lett.*, 80:849–852, Jan 1998.

[5] P. J. Metaxas, J.-P. Jamet, A. Mougin, M. Cormier, J. Ferré, V. Baltz, B. Rodmacq, B. Dieny, and R. L. Stamps. Creep and Flow Regimes of Magnetic Domain-Wall Motion in Ultrathin Pt/Co/Pt Films with Perpendicular Anisotropy. *Phys. Rev. Lett.*, 99:217208, Nov 2007.

[6] A Fraile Rodríguez, L J Heyderman, F Nolting, A Hoffmannand J E Pearson, L M Doeswijk, M A F van den Boogaart, and J Brugger. Permalloy thin films exchange coupled to arrays of cobalt islands. *Appl. Phys. Lett.*, 89:142508, 2006.

[7] G Rodríguez-Rodríguez, A Pérez-Junquera, M Vélez, J V Anguita, J I Martín, H Rubio, and J M Alameda. MFM observations of domain wall creep and pinning effects in amorphous Co_xSi_{1-x} films with diluted arrays of antidots. *J. Phys. D: Appl. Phys.*, 40:3051–3055, 2007.

[8] A. Pérez-Junquera, V. I. Marconi, A. B. Kolton, L. M. Álvarez-Prado, Y. Souche, A. Alija, M. Vélez, J. V. Anguita, J. M. Alameda, J. I. Martín, and J. M. R. Parrondo. Crossed-Ratchet Effects for Magnetic Domain Wall Motion. *Phys. Rev. Lett.*, 100(3):037203, 2008.

Asymmetric magnetic domain wall propagation   19

[9] Lili Ji, A. Orlov, G.H. Bernstein, W. Porod, and G. Csaba. Domain-wall trapping and control on submicron magnetic wire by localized field. In *9th IEEE Conference on Nanotechnology, 2009. IEEE-NANO 2009.*, pages 758–762, 2009.

[10] L. O'Brien, D. Petit, E. R. Lewis, R. P. Cowburn, D. E. Read, J. Sampaio, H. T. Zeng, and A.-V. Jausovec. Tunable Remote Pinning of Domain Walls in Magnetic Nanowires. *Phys. Rev. Lett.*, 106:087204, Feb 2011.

[11] Lili Ji, Alexei Orlov, Gary H Bernstein, Wolfgang Porod, and Gyorgy Csaba. Domain-wall trapping and control on submicron magnetic wire by localized field. In *Nanotechnology, 2009. IEEE-NANO 2009. 9th IEEE Conference on*, pages 758–762. IEEE, 2009.

[12] Jeroen H. Franken, Mark A. J. van der Heijden, Tim H. Ellis, Reinoud Lavrijsen, Carsten Daniels, Damien McGrouther, Henk J. M. Swagten, and Bert Koopmans. Beam-Induced Fe Nanopillars as Tunable Domain-Wall Pinning Sites. *Advanced Functional Materials*, 24:3508–3514, 2014.

[13] R. A. van Mourik, C. T. Rettner, B. Koopmans, and S. S. P. Parkin. Control of domain wall pinning by switchable nanomagnet state. *J. Appl. Phys.*, 115(17):17D503, May 2014.

[14] M. Gottwald, M. Hehn, D. Lacour, T. Hauet, F. Montaigne, S. Mangin, P. Fischer, M.-Y. Im, and A. Berger. Asymmetric magnetization reversal in dipolarly coupled spin valve structures with perpendicular magnetic anisotropy. *Phys. Rev. B*, 85:064403, Feb 2012.

[15] J. Nogués and I. K. Schuller. Exchange bias. *J. Magn. Magn. Mater.*, 192:203, 1999.

[16] R. L. Stamps. Mechanisms for exchange bias. *J. Phys. D: Appl. Phys*, 33:R247, 2000.

[17] M Kiwi. Exchange bias theory. *J. Magn. Magn. Mater.*, 234:584, 2001.

[18] M D Stiles and R D McMichael. Coercivity in exchange-bias layers. *Phys. Rev. B*, 63:064405, 2001.

[19] Stuart S. P. Parkin, Masamitsu Hayashi, and Luc Thomas. Magnetic Domain-Wall Racetrack Memory. *Science*, 320:190–194, 2008.

[20] Tetsuhiro Suzuki, S. Fukami, K. Nagahara, Norikazu Ohshima, and N. Ishiwata. Evaluation of Scalability for Current-Driven Domain Wall Motion in a Co/Ni Multilayer Strip for Memory Applications. *IEEE Trans. Mag.*, 45(10):3776–3779, 2009.

[21] D. A. Allwood, G. Xiong, C. C. Faulkner, D. Atkinson, D. Petit, and R. P. Cowburn. Magnetic Domain-Wall Logic. *Science*, 309:1688–1692, 2005.

[22] J. Moritz, F. Garcia, J. C. Toussaint, B. Dieny, and J.-P. Nozières. Orange peel coupling in multilayers with perpendicular magnetic anisotropy:Application to (Co/Pt)-based exchange-biased spin-valves. *Europhys. Lett.*, 65:123, 2004.

[23] A. Lyberatos, J. Earl, and R. W. Chantrell. Model of thermally activated magnetization reversal in thin films of amorphous rare-earth-transition-metal alloys. *Phys. Rev. B*, 53:5493–5504, Mar 1996.

[24] A Lyberatos. Monte Carlo models of the magnetization reversal in thin films with strong perpendicular anisotropy. *Journal of Physics D: Applied Physics*, 33(13):R117, 2000.

[25] Hong Ji and Mark O. Robbins. Transition from compact to self-similar growth in disordered systems: Fluid invasion and magnetic-domain growth. *Phys. Rev. A*, 44:2538, 1991.

[26] Sug-Bong Choe and Sung-Chul Shin. Phase diagram of three contrasting magnetization reversal phases in uniaxial ferromagnetic thin films. *Applied Physics Letters*, 80(10):1791–1793, 2002.

[27] J. Ferré. In B. Hillebrands and K. Ounadjela, editors, *Spin Dynamics in Confined Magnetic Structures I*. Springer, 2002.